Accepted Manuscript

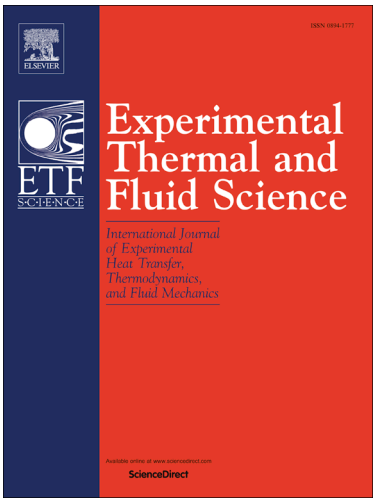

Spanwise flow development within a laminar separation bubble under natural and forced transition

Theodoros Michelis, Marios Kotsonis, Serhiy Yarusevych

PII: S0894-1777(18)30300-5
DOI: https://doi.org/10.1016/j.expthermflusci.2018.02.032
Reference: ETF 9393

To appear in: *Experimental Thermal and Fluid Science*

Received Date: 8 September 2017
Accepted Date: 26 February 2018

Please cite this article as: T. Michelis, M. Kotsonis, S. Yarusevych, Spanwise flow development within a laminar separation bubble under natural and forced transition, *Experimental Thermal and Fluid Science* (2018), doi: https://doi.org/10.1016/j.expthermflusci.2018.02.032

Spanwise flow development within a laminar separation bubble under natural and forced transition

Theodoros Michelis[a], Marios Kotsonis[a], Serhiy Yarusevych[b]

[a] *Faculty of Aerospace Engineering, Delft University of Technology, Kluyverweg 2, 2629HT, Delft, The Netherlands*
[b] *Department of Mechanical and Mechatronics Engineering, University of Waterloo, 200 University Ave. W, Waterloo, Ontario, Canada, N2L 3G1*

Abstract

The variation of streamwise and spanwise characteristic wavelengths of a NACA 0018 laminar separation bubble under natural and periodic excitation conditions is investigated experimentally. Periodic forcing is applied with an AC-DBD plasma actuator, and the response of the bubble is characterised in two orthogonal planes by means of time-resolved particle image velocimetry. Periodic excitation results in substantial time-averaged size reduction of the bubble. Linear stability analysis is used to establish that the most notable flow deformation is achieved when excitation is applied at the most unstable frequency, which does not significantly vary ($< 4\%$) for the range of excitation parameters investigated. At excitation frequencies well below the unstable frequency band, the shear layer does not lock to the excitation and is, instead, modulated. Lock-in is achieved at higher forcing frequencies, which are within the unstable band. For the case of modulated shedding, spanwise deformations become more significant than in the natural case; whereas when shedding becomes locked to the excitation frequency, the coherence of the rollers along the span increases. Characteristic streamwise and spanwise wavelengths are statistically quantified by means of spatial wavelet analysis, demonstrating that spanwise deformations attain wider range of wavelengths than the respective streamwise rollers. Analysis of these results suggests that spanwise deformation is associated to both the incoming boundary layer and shear layer stability characteristics.

Keywords: Laminar separation bubble, linear stability theory, PIV, POD

1. Introduction

A Laminar Separation Bubble (LSB) develops if a laminar boundary layer is subjected to a sufficiently strong adverse pressure gradient [1]. This causes separation, with subsequent laminar to turbulent transition of the shear layer. Increased mixing of the separated shear layer results in time-averaged reattachment, thus forming a closed recirculation region, namely the LSB [e.g. 2, 3, 4]. This phenomenon is common on the suction side of airfoils at low Reynolds numbers based on chord length ($Re_c \lesssim 500,000$). It is relevant for a variety of industrial applications spanning from unmanned aerial vehicles to gliders and wind turbine blades. Since an LSB is inherently unstable, it can lead to unwanted dynamic effects such as abrupt stall and noise production. Consequently, detailed description of the dynamics of LSBs is essential in order to effectively control them and has been a topic of extensive studies [e.g. 5, 6, 7, 8, 9].

It has been established that transition in the separated shear layer is governed by convective amplification of Kelvin-Helmholtz disturbances [10, 11]. Once the velocity fluctuations are amplified sufficiently ($u/U_0 \approx 10\%$ [12]), shear layer roll-up takes place and vortices are shed in the aft portion of the bubble. These structures undergo relatively rapid spanwise deformations and break down to smaller scales in the vicinity of the mean reattachment location [11]. Kurelek et al. [13] link the localised vortex breakdown and the subsequent transition to turbulence to the spanwise deformation of the vortex filaments. Marxen et al. [11] suggest that several instability mechanisms acting individually or in combination may be responsible for the vortex breakdown, including elliptic instability of the spanwise rollers and hyperbolic instability of the streamwise filaments connecting the main vortices. Several studies also suggest that the later stages of transition in the separation bubble are related to the development of natural perturbations in the attached boundary layer upstream of separation [e.g. 7, 14]. In applications with relatively high free stream turbulence intensity, e.g. in turbomachinery [15, 16], strong streamwise streaks form in the boundary layer, significantly perturbing the development of the shear layer in the separation bubble and thereby affecting the transition process [17, 18]. Rao et al. [18] also show that similar streaks can be produced due to localised roughness. Michelis et al. [19] postulate that, in general, the initial spanwise deformation in shear layer rollers, developing in LSBs, can be conditioned by a superposition of fundamental normal and oblique instability modes in the incoming laminar boundary layer. In a simplified model, they demonstrate that spanwise coherence and deformation of spanwise structures is affected, by the relative magnitudes of these archetypal modes.

A number of previous investigations considered flow control aimed at reducing the size of the separation region by means of periodic forcing. Examples of different types of forcing employed include external acoustic excitation [6], synthetic jets [15], surface actuation [20], and plasma actuators [21]. In addition, a number of studies focused on stability of LSBs, utilised either periodic [22, 23] or impulsive [1, 4] forcing. The general consensus is that forcing at the most amplified frequency in the

unforced bubble leads to the most significant diminishing of the bubble for a given excitation amplitude [23], although the most unstable frequency decreases moderately as the bubble size is reduced [21]. Notwithstanding the strong three-dimensionality of the bubble, especially in the roll-up and reattachment region, the majority of the available experimental investigations involve two-dimensional description of the bubble topology in the streamwise, wall-normal plane. The details of the spatio-temporal flow development in LSBs along the spanwise direction has been considered only in a limited number of studies [e.g. 24, 25, 19], therefore, the effect of controlled perturbations on *both* the streamwise and spanwise features of flow development and transition merits further investigation.

This work focuses on streamwise and spanwise characterisation of an LSB under natural and forced conditions. Periodic forcing of the LSB by means of a Dielectric Barrier Discharge (DBD) plasma actuator is applied in order to assess the effect of forced perturbations on the bubble dynamics. The disturbance is introduced locally, upstream of mean separation and in a two-dimensional manner. Emphasis is placed on the combined quantitative description of the streamwise and spanwise flow development, particularly the formation and evolution of coherent structures for which strong three-dimensional effects are expected in the aft portion of the bubble [11]. To enable such description, the resulting spatial and temporal response of the flow-field is captured with streamwise- and spanwise-oriented time-resolved, two-component, Particle Image Velocimetry (PIV) measurements.

2. Experimental setup

Experiments are carried out in a closed-loop wind tunnel with square cross-section of 610mm×610mm. A NACA 0018 airfoil of 200mm chord and 610mm span is inserted in the test section (figure 1). The airfoil is set at a geometric and aerodynamic angle of attack of 4° while the pressure side boundary layer is tripped by means of a three-dimensional roughness strip. This is done in order to avoid laminar separation and consequently unsteady effects as well as trailing edge tonal noise emission [26]. The freestream velocity is set to $U_0 = 9.2\text{m/s}$ resulting in a Reynolds number based on the chord of $Re_c = 126,000$. At this speed, the freestream turbulence intensity is approximately 0.1% within a frequency range of 0Hz to 10kHz. For the selected conditions, a laminar separation bubble forms on the suction side, with mean separation and reattachment points at $x/c \approx 0.35$ and 0.53, respectively.

The laminar boundary layer is perturbed by means of an Alternating Current Dielectric Barrier Discharge (AC-DBD) plasma actuator [27, 28, 29], positioned along the span of the airfoil. It consists of two asymmetrically placed self-adhesive copper electrodes separated by a *Kapton*® dielectric layer. The electrodes are 10mm wide in the streamwise direction, 30µm thick and 300mm long in the spanwise direction, while the dielectric barrier is 120µm thick. Preliminary surface pressure measurements indicated negligible influence of the actuator protuberance on the position or dynamics of the LSB. The discharge gap is located at $x/c = 0.3$, upstream of the separation point. The forcing

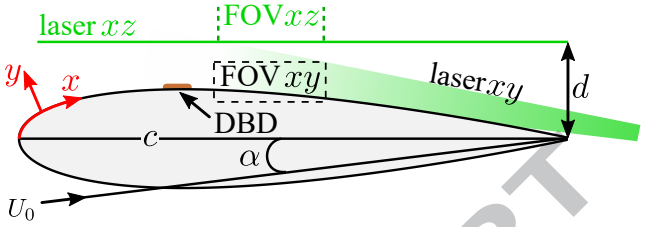

Figure 1: Experimental arrangement. The green dashed vertical lines denote the streamwise extent of the spanwise field of view (FOV).

Table 1: PIV parameters for the two measurement planes.

Parameter	$x-y$ plane	$x-z$ plane
Magnification factor	0.32	0.36
Field of view [pixels]	473×161	247×247
Field of view [mm^2]	65×22	56×56
Sampling rate [Hz]	2000	2000
Frame separation [µs]	40	60
Freestream displacement [pixels]	13	10
Number of samples	5457	2728
Vector pitch [mm]	0.14	0.23

signal is comprised of repetitive short pulses that are constructed by modulating a 3.5kV$_{pp}$ and 5kHz sinusoidal carrier signal with a square signal of selected frequency. The modulation duty cycle is adjusted with respect to the required pulse excitation frequency ($f_e^+ = f_e c/U_0$) to maintain a pulse width of 1ms.

Time-resolved Particle Image Velocimetry (PIV) measurements are carried out by employing two *Photron SA4* high-speed cameras with 200mm Nikkor macro lenses, set at to aperture of $f/5.6$. Illumination is performed by a *Photonics DM20-527* Nd:YLF laser, whose beam is transformed to an approximately 1.5mm thick light sheet. Flow seeding is provided by a fog generator that uses water-glycol mixture, delivering droplets of 1µm in diameter.

The velocity measurements are performed in two fields of view, as shown in figure 1. The first lies in the $x-y$ plane, at the airfoil midspan and is constructed by overlapping the field of view of two cameras, obtaining a combined field of view of 65mm × 22mm. The second view lies in the $x-z$ plane, parallel to and at a distance of $d = 21$mm from the airfoil chord. Here, images are recorded with a single camera, capturing a field of view of 56mm × 56mm. In both cases, particle images are acquired in double frame mode at an acquisition frequency of 2kHz. The acquired image pairs are then processed with *LaVision Davis 8.2* software, using a multi-step interrogation algorithm [30] with an initial window size of 48×48 pixels and a final size of 16×16 pixels with 75% overlap. As a result, vector fields of 473×161 and 247×247 vectors are obtained for side and top views, respectively. Table 1 summarises the PIV parameters for both measurement planes.

The results are presented on a surface-attached coordinate system (figure 1). The x coordinate runs tangent to the airfoil

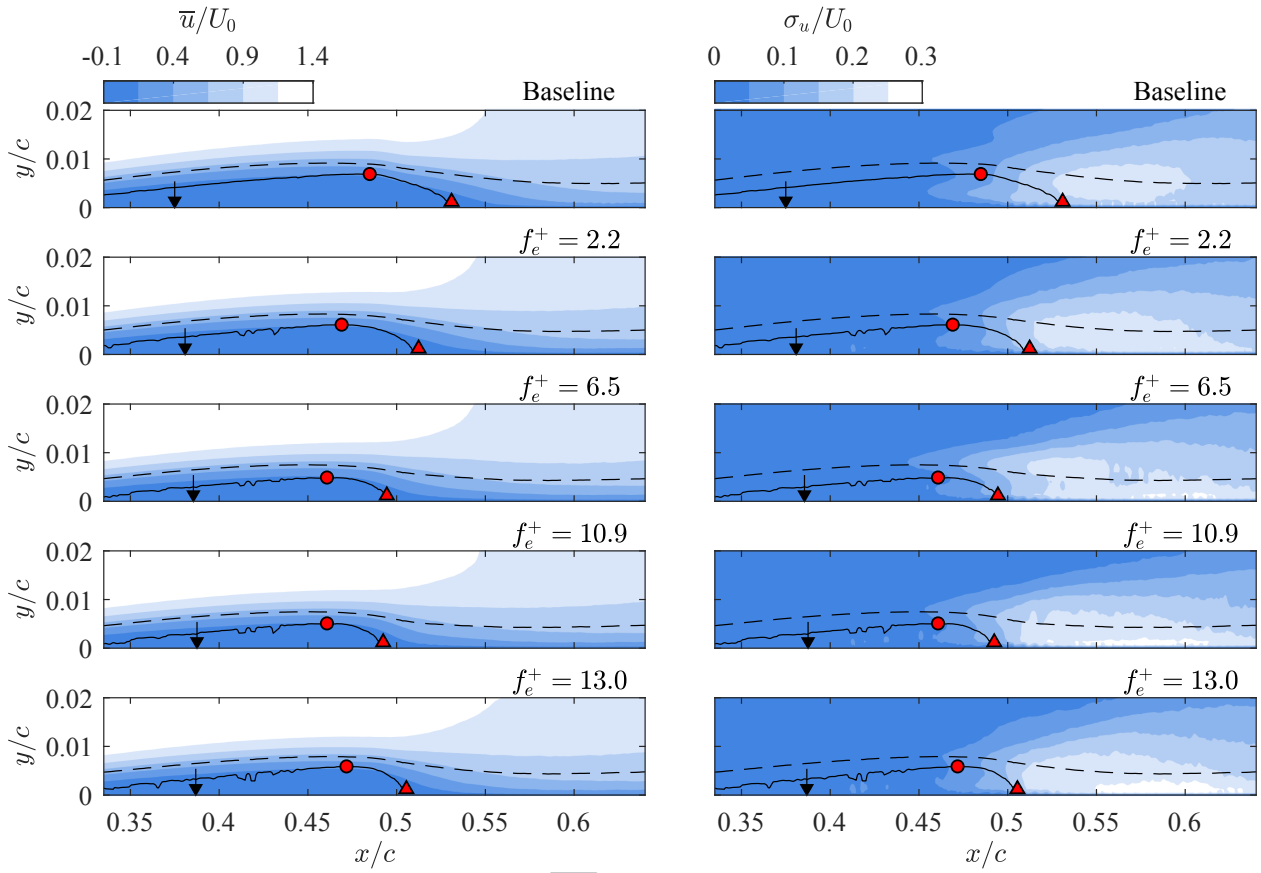

Figure 2: *First column*: mean streamwise velocity, *second column:* standard deviation of streamwise velocity. Solid and dashed lines correspond to the dividing streamline and displacement thickness, respectively. The triangle and circle correspond to the mean reattachment and maximum mean bubble height, respectively. The arrows indicate the midpoint between the maximum bubble height location and the linearly extrapolated mean separation point.

surface with an origin at the leading edge. In turn, the y coordinate is locally normal to and measured from the airfoil surface. The required scaling and geometric transformation of the vector fields (dewarping) is applied to all instantaneous realisations of the measurements in the $x-y$ plane. For the $x-z$ plane measurements, no dewarping is applied. The z coordinate is running parallel to the airfoil leading edge, with an origin at the midspan of the model. Finally, lengths are scaled with the airfoil chord and velocities with the free stream velocity.

3. Results

3.1. Steady state features on the $x-y$ plane

Figure 2 illustrates the effect of repetitive harmonic excitation on the time-averaged velocity field at several frequencies. Dashed lines in the figures represent the boundary layer displacement thickness, δ^*, while solid black lines mark the dividing streamline, which outlines the location of the separation bubble. The mean velocity contours for the baseline case demonstrate that periodic excitation reduces both the length and maximum height of the separation bubble, with the maximum reduction achieved at $f_e^+ = 10.9$. This is attributed primarily to the upstream motion of the mean reattachment location. The standard deviation contours demonstrate that the reduction in the length of the bubble is accomplished due to an earlier onset of velocity fluctuations in the separated shear layer. The observed trends in the mean bubble topology are similar to those reported for a NACA 0012 airfoil subjected to controlled harmonic perturbations in Yarusevych and Kotsonis [23].

To better visualise the mean flow deformation caused by forcing and its effect on the separating boundary layer, the displacement thickness, δ^* and the shape factor, H, for representative cases are provided in figure 3. Evidently, the increase of forcing frequency causes a reduction of bubble size, though little differences are observed between $f_e^+ = 6.5$ and $f_e^+ = 10.9$. Nonetheless, the overall reduction of δ^* for increasing forcing frequency (figure 3a) is expected to affect the growth of disturbances in the separated shear layer. This is further discussed in section 3.3. In turn, H exhibits elevated values up to the mean maximum height (figure 3b), a behaviour typical for boundary layers under adverse pressure gradient. The value of the shape factor drops to $H = 1.7$ downstream reattachment, representative of a turbulent boundary layer. Note that there is no correspondence to a fully developed turbulent profile (log-law) as relaxation requires several bubble lengths [31].

3.2. Spatio-temporal characteristics on the $x-y$ plane

The main focus of the present study is on the changes in bubble dynamics produced by the excitation. To illustrate the

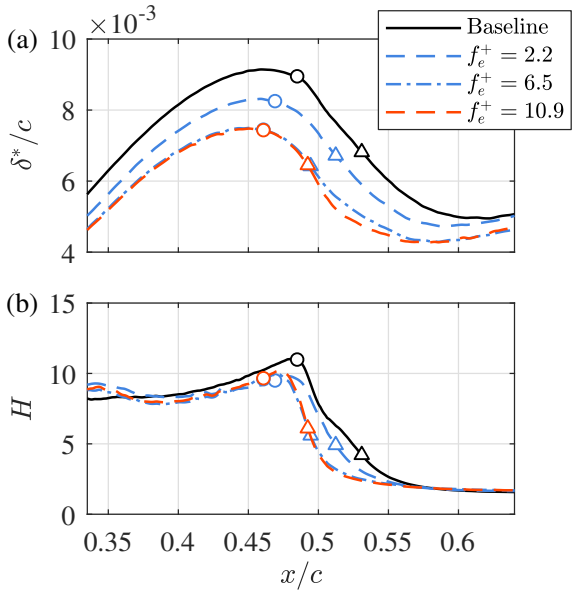

Figure 3: (a) Displacement thickness, δ^*, and (b) shape factor H for representative forcing cases. Circles and triangles indicate the location of the mean maximum height and mean reattachment, respectively.

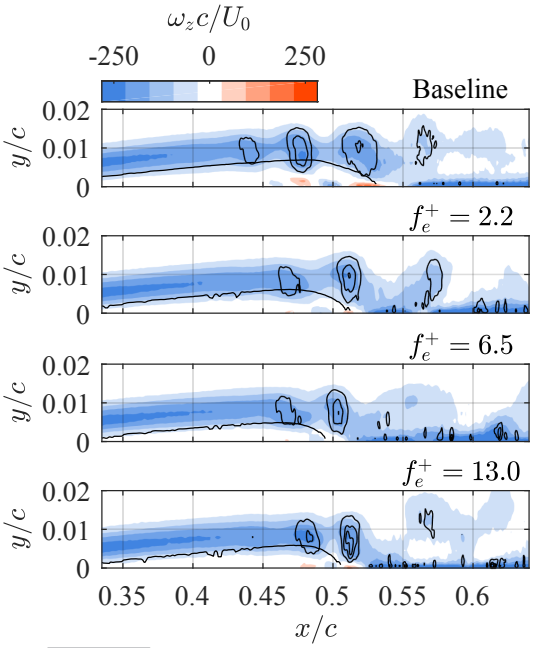

Figure 4: Instantaneous fields of spanwise vorticity in the $x-y$ plane at selected excitation frequencies. Solid lines correspond to the mean dividing streamline. In addition, superimposed contours of Q criterion are provided, indicating the streamwise location of rollers.

unsteady flow development in the separation bubble, figure 4 presents instantaneous snapshots of spanwise vorticity contours for the baseline case and selected forcing frequencies. Additional insight into the illustrated flow dynamics can be gained through the corresponding video sequences available as supplementary material. For the baseline flow, shedding of shear layer vortices is observed in the aft portion of the separation bubble. The shear layer roll-up occurs in the vicinity of the streamwise location of the maximum bubble height, highlighting the key role played by the resulting large scale structures in the subsequent mean flow reattachment. The approximate streamwise wavelength of the shed vortices, scaled with the displacement thickness at separation ($\delta_s^* = 0.63$mm), is $\lambda_x/\delta_s^* \approx 15.92$, which is subject to the natural cycle-to-cycle variations. This is in reasonable agreement with the observations in other studies with similar Reynolds numbers and displacement thickness at separation [e.g. 23, 16]. Note that occasional, non-periodic merging of these structures can take place.

When the plasma excitation is applied, the shear layer roll-up occurs earlier upstream, with changes in roll-up location correlating with those in the position of maximum bubble height relative to that for the baseline case (figure 2). The dynamics within the aft portion of the laminar separation bubble are governed by the shedding of shear layer vortices. Strikingly, despite notable effect produced by the excitation on the mean bubble topology and the substantial differences in the excitation frequencies, the average streamwise wavelength of the shear layer rollers does not change significantly (figure 4), which is confirmed quantitatively in section 3.6. The small variation of streamwise wavelength is due to the fact that vortex shedding does not lock onto the excitation frequency for all the cases considered, which is examined in detail in the following sections. Instead, excitation at lower frequencies is found to cause frequency modulation of the shear layer shedding.

The spectral content of dominant velocity fluctuations in the separated shear layer is analysed in figure 5, where frequency spectra of wall-normal velocity fluctuations, sampled at the streamwise location of maximum bubble height and the wall-normal location corresponding to the displacement thickness, are presented. Power Spectral Density (PSD) is estimated via the Welch method [32] by dividing the temporal signal into 5 windows with 50% overlap, leading to a spectrum with frequency resolution of $F^+ = 0.021$. The results pertaining to the baseline case show that the most energetic velocity fluctuations occur within a relatively broad band of frequencies centred at approximately $F^+ = 13.0$. When periodic excitation is applied, the spectra feature a strong peak at the excitation frequency. However, at excitation frequencies substantially lower than the frequency of the dominant fluctuations in the unexcited flow, namely, $f_e^+ = 2.2$ and 4.3, strong amplification of harmonics takes place up to the harmonic frequency closest to $F^+ = 13.0$. At the same time, the spectra retain significant energy content distributed around the band of frequencies amplified in the unexcited flow. As the excitation frequency increases towards the frequency of the dominant fluctuations in the unexcited flow, the broad-band energy content associated with the naturally unstable frequencies around $F^+ = 13.0$ progressively diminishes. For $f_e^+ = 6.5$, dominant velocity fluctuations are associated with the excitation frequency and its first harmonic, with a similar result observed at $f_e^+ = 8.7$. At $f_e^+ = 10.9$, the fluctuations are concentrated at the excitation frequency, while at $f_e^+ = 13.0$ spectral content is prominent in the unstable frequency range.

Similar results can be deduced from wavenumber-frequency spectra (figure 6). To obtain the latter, a wall-normal velocity sig-

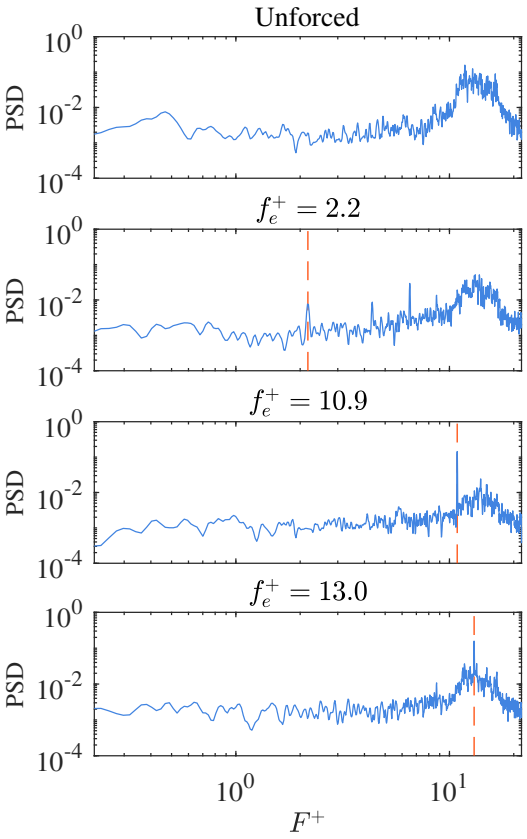

Figure 5: Power spectral density [db/F^+] of wall-normal velocity fluctuations sampled at the streamwise location of the maximum bubble height and at a wall-normal distance of the corresponding displacement thickness.

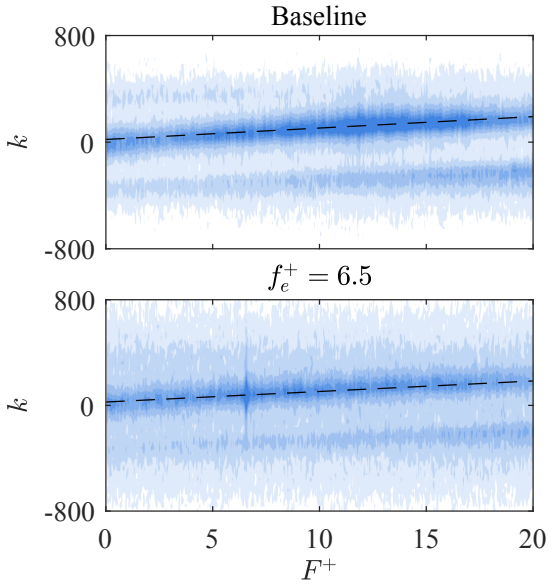

Figure 6: Wavenumber-frequency spectra computed along a constant wall-normal distance corresponding to the displacement thickness at the maximum bubble height.

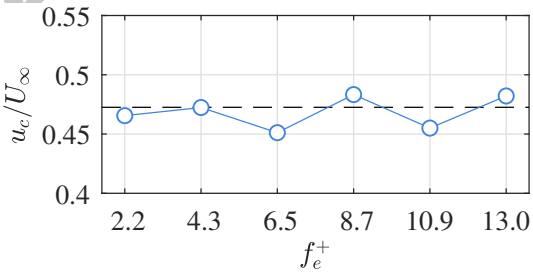

Figure 7: Convective speed estimated through the wavenumber-frequency spectra. The dashed line indicates the baseline case.

nal is extracted at multiple locations along the streamwise direction, at a wall-normal distance corresponding to the displacement thickness of the mean bubble height. A two-dimensional power spectral density estimate is subsequently determined based on the Welch method [32], for which the extracted signal is divided into six and two windows with 75% overlap for the temporal and spatial dimensions, respectively. As evident in figure 6, the strong spectral content is aligned along a well-defined convective ridge, marked by dashed lines in the figure, signifying the convective nature of pertinent perturbations in the flow. The slope of the convective ridge can be used to estimate the convective velocity of the dominant structures, shown in figure 7. When scaled with the freestream velocity, the convective speed is $u_c/U_\infty = 0.47$ for the unforced case and lies in the interval $0.45 < u_c/U_\infty < 0.48$ when excitation is applied. These results are in excellent agreement with similar studies [e.g. 5, 26, 4, 16] and pertain to the convective nature of instabilities in laminar separation bubbles with mild to low maximum reverse flows ($< 0.05U_\infty$) [e.g. 31, 33, 23].

Evidently, the convective velocity of dominant disturbances in the separated shear layer does not change significantly with excitation frequency, which allows for a comparative analysis of spectral results in figure 5 and vorticity sequences in figure 4. As pointed out earlier, the characteristic streamwise wavelength of shear layer vortices does not change significantly between the baseline and excited flow cases. Thus, excitation at relatively low excitation frequencies, namely, $2.2 \leq f_e^+ \leq 6.5$, does not lock the shedding frequency to the excitation frequency. Instead, as further discussed in section 3.5, a large scale modulation of the shedding process, synchronised to the impulses, is observed. Hence, strong peaks are produced in the velocity spectra at the excitation frequency and its harmonics up to the mean shedding frequency. The shear layer shedding frequency begins to lock onto the excitation frequency only when the latter approaches the frequency of the most amplified perturbations, which occurs at $f_e^+ = 8.7$ in the present study and becomes most prominent for $f_e^+ = 10.9$ and 13.0.

3.3. *Linear stability analysis*

Linear stability analysis is performed on the measured mean velocity by solving the Orr-Sommerfeld equation in a convective formulation, following the methodology described in Mack [34] and van Ingen and Kotsonis [35]. For the cases considered, mean velocity profiles are extracted at the location laying at the midpoint between mean separation and mean maximum bubble height (see figure 2). This location has been selected over the

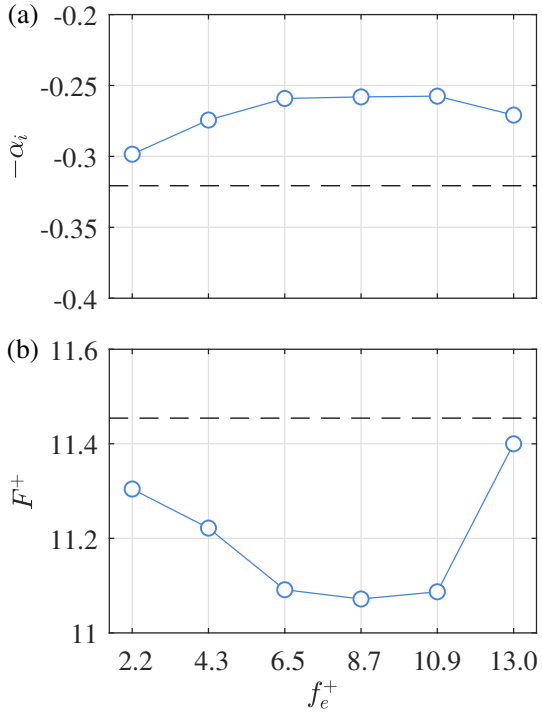

Figure 8: Linear stability analysis results pertaining to at the midpoint between separation and maximum bubble height streamwise locations (see figure 2). (a) Maximum growth rate and (b) most unstable frequency. The dashed line corresponds to the baseline case.

maximum displacement point as, at the latter, non-linear effects and spanwise deformations become more prevalent (see figure 9), rendering linear stability analysis results less reliable. In addition, the shedding wavenumber parameter, $kl = 2\pi/\lambda_x$ [36, 16], is estimated, where l is the shear layer thickness at separation. The results yield $kl \approx 0.77$, close to the value characterising free mixing layers where $kl \approx 0.8$ [36]. Consequently, the typical Kelvin-Helmholtz instability features are observed.

The minimum local growth rate ($-\alpha_i$) and the corresponding most unstable frequency are depicted in figure 8 for all forcing frequencies. It can be seen that the most unstable frequency of the baseline flow is approximately $F^+ = 11.4$. Both the band of unstable frequencies and the frequency of the most amplified disturbances are within reasonable agreement with the frequencies of measured shear layer velocity fluctuations (figure 5). When the flow is excited by controlled perturbations, the reduced size of the bubble causes a decrease in the growth rate (figure 8a), consistent with the effect of mean flow deformations reported by Marxen et al. [37] and Yarusevych and Kotsonis [23]. However, the frequency of the most amplified disturbances does not change as significantly (figure 8b). It decreases from $F^+ = 11.4$ for the baseline case to about $F^+ = 11.1$ when excitation is applied at $f_e^+ = 10.9$. The results confirm that the observed response of the bubble (figure 5) is governed by the attendant stability characteristics, with excitation being capable to lock the shedding of vortices, originating from growing perturbations in the separated shear layer, only when it is applied sufficiently close to the frequency of the most unstable perturbations. Instead, at forcing frequencies significantly lower than the natural shedding frequency, the shedding process remains largely uninterrupted between forcing pulses. For a given forcing amplitude, artificial perturbations attain the highest amplitude when they are introduced at the most unstable frequency, which is why the most notable reduction in the mean extent of the separation bubble is attained at $f_e^+ = 10.9$ (figure 2).

3.4. Spatio-temporal characteristics on the $x-z$ plane

Further analysis of the changes in separation bubble dynamics due to harmonic excitation is performed by considering the spanwise development of separated shear layer rollers. Figure 9 presents time instants of streamwise velocity contours for the baseline and selected excitation cases, as measured by the spanwise PIV. Corresponding video sequences are also available as supplementary material. For these results, the location of the spanwise measurement plane is selected such that it passes through the top of the shear layer rollers. However, it should be stressed that the distance of the measurement plane from the airfoil surface is changing with x (figure 1).

The presence of dominant shear layer vortices is identified by high magnitudes of streamwise velocity. For the baseline case (figure 9a), the initial shear layer roll-up is strongly uniform along the span. As the vortices convect downstream, they develop notable spanwise deformations and break down in the vicinity of the mean reattachment location. Similar flow development is observed for the excited flow cases, although the development of the rollers occurs within a shorter streamwise extent as the mean bubble size is reduced. At lower excitation frequencies (figures 9b, c), modulations of the shedding by the excitation appears to produce more significant spanwise deformations, compared to higher excitation frequencies. In contrast, when the shedding locks to the excitation frequency (figure 9d), the rollers tend to retain spanwise coherence further downstream. Kurelek et al. [13] suggest that spanwise vortex deformations lead to localised vortex breakup, and are hence of interest to the flow development during the later stages of transition in the aft portion of the separation bubble.

3.5. Proper orthogonal decomposition

A quantitative analysis of the excitation effect on the characteristics of dominant coherent structures is performed based on Proper Orthogonal Decomposition [38] of the fluctuating velocity in the $x-z$ measurement plane. Figures 10a and 10b show the modal energy distribution and cumulative energy, respectively, obtained on the $x-z$ fields. The results suggest strong pairing of the two most energetic modes, as evident by their very similar energy levels. This was confirmed by cross-correlation of their respective temporal coefficients (not shown here for brevity). These harmonically coupled pairs are typical for periodic coherent structures in convective flows [39]. In the same fashion, pairing between the third and fourth most energetic modes is also observed, albeit at much lower energy levels, especially for the high frequency forcing. In general, it is evident that forcing frequencies below $f_e^+ = 6.5$ tend to reduce the energy of the first pair and increase the energy of the second pair compared to the

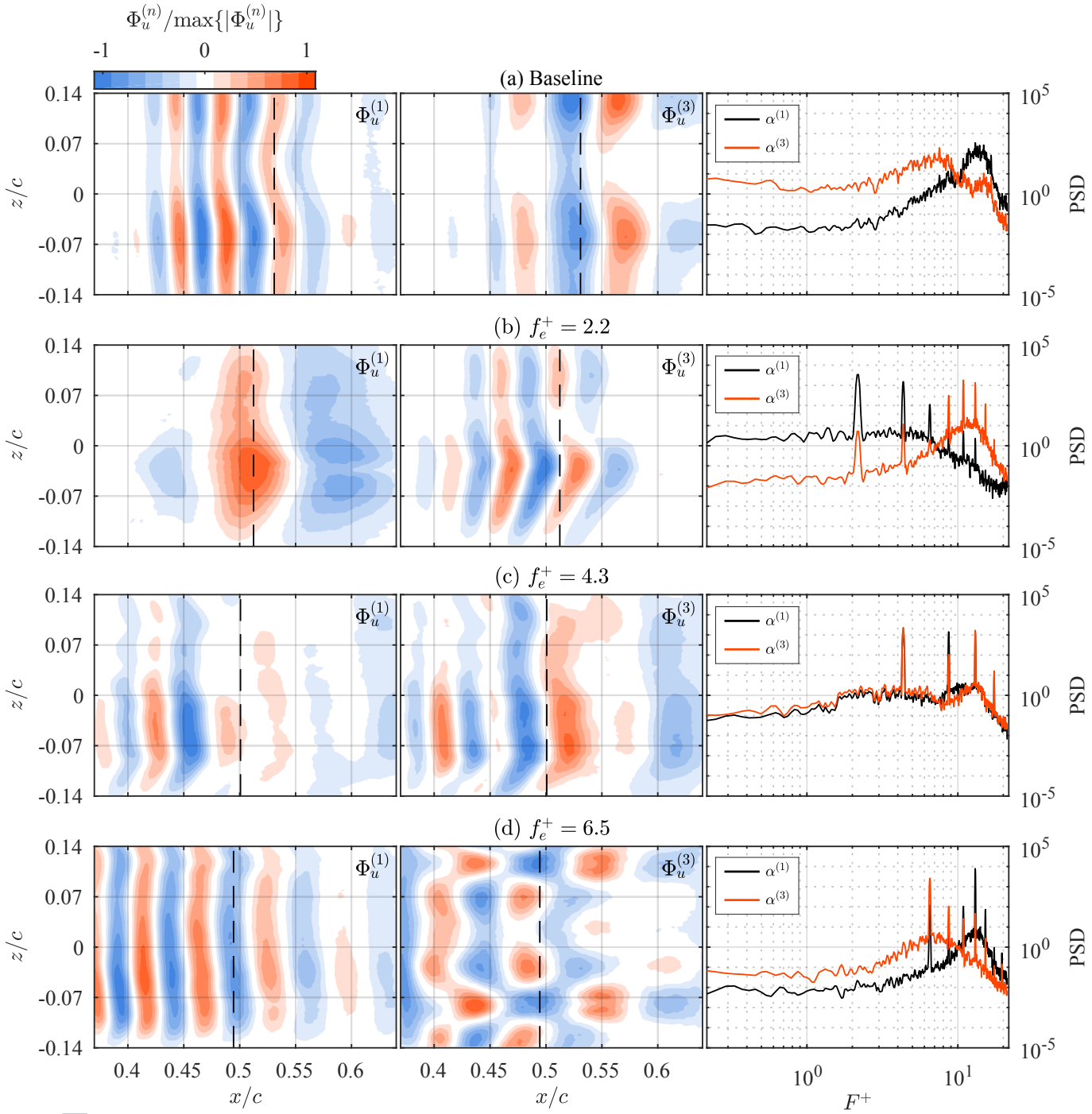

Figure 11: Streamwise component of the POD spatial eigenfunctions Φ_1 and Φ_3 on the $x-z$ plane, along with the frequency spectra of the corresponding temporal coefficients in dB/F^+. The dashed lines indicate the location of mean reattachment.

unforced baseline. In contrast, forcing frequencies close to the natural shedding frequency of the bubble strongly enhance the energy content of the first pair and diminish all other modes.

The structure of the corresponding spatial modes and frequency spectra of their temporal coefficients are presented in figures 11 and 12. Considering the baseline case, the first two most energetic modes capture the coherent shedding of the shear layer vortices, as can be seen from the similarity of the streamwise wavelength between $\Phi^{(1)}$ (figure 11a) and instantaneous snapshots (figures 4 and 9). The spanwise amplitude modulation of the rollers observed here is attributed to non-uniform spanwise distribution of natural disturbances typical for experimental conditions, thus affecting the spanwise breakdown of the rollers as observed in other studies [40, 25, 13]. The spectrum of the corresponding temporal coefficient shows a broad peak within the same band of frequencies as that encompassed by the dominant broad peak in wall-normal velocity spectra measured in the $x-y$ plane (figure 5). The second mode pair (modes 3

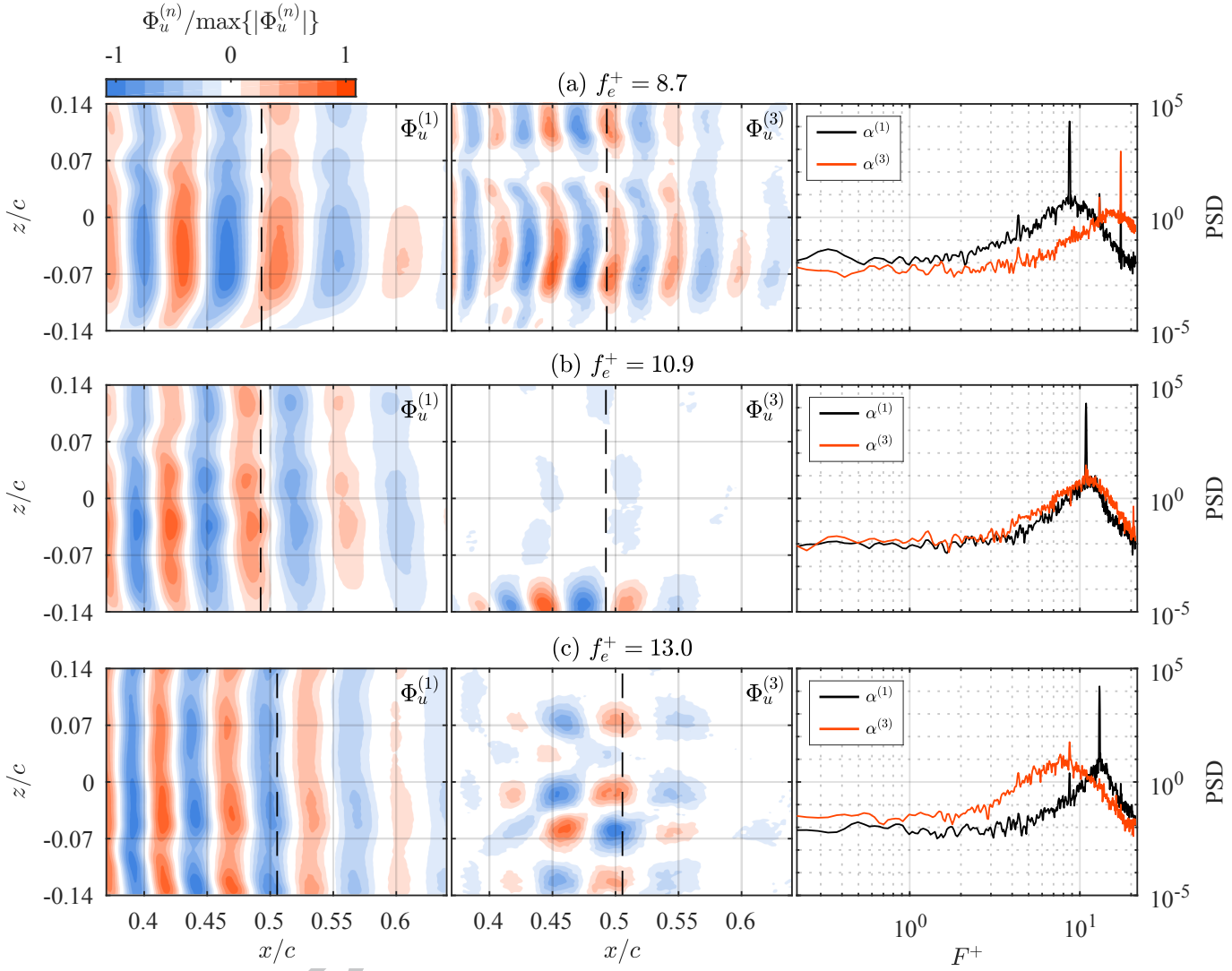

Figure 12: Streamwise component of the POD spatial eigenfunctions Φ_1 and Φ_3 on the $x-z$ plane, along with the frequency spectra of the corresponding temporal coefficients in dB/F^+. The dashed lines indicate the location of mean reattachment.

and 4) features a spatially periodic topology with nearly double the streamwise wavelength in the aft portion of the bubble and half the dominant frequency, attributed to the subharmonic of the fundamental frequency. This may be attributed to vortex merging taking place downstream of the shear layer roll-up.

When excitation is applied at $f_e^+ = 2.2$ (figure 11b), the dominant mode pair captures a spatially periodic topology in the aft portion of the bubble and largely downstream of mean reattachment. While the pairing of the two first POD modes suggests that this is produced by convective, coherent structures, inspection of the $x-y$ velocity planes (figure 4) reveals no clearly discernible vortical structures of comparable wavelength. Instead, the most energetic POD mode pair corresponds to a large scale modulation of the shedding process, synchronised to the impulsive forcing. This is confirmed by the spectra of the temporal coefficient of mode 1, which are dominated by narrow peaks at the forcing frequency and its harmonics, a feature which is typical of impulsively modulated signal response [41]. In contrast, the second mode pair reflects the actual shedding, occurring at the most unstable frequency of the bubble. These observations confirm that low frequency excitation modulates the natural shedding rather than shifting its frequency. Thus, stronger vortices are produced at each pulse which contribute more substantially to the overall fluctuating energy content than the non-actuated perturbations. Globally, the excitation leads to reallocation of the relative energy content between the two most energetic more pairs compared to the baseline case (figure 10).

As the excitation frequency is increased to $f_e^+ = 4.3$ (figure 11c), both mode pairs feature dual broad peaks in the spectra of their temporal coefficients. The lower frequency peak is associated with the excitation frequency. The higher frequency peak is approximately bound by the two higher harmonics of the excitation frequency, falling within the most unstable frequency band. Such a harmonic excitation occurs in this case due to the close proximity of both first and second harmonics of the excitation frequency to the band of natural most unstable frequencies

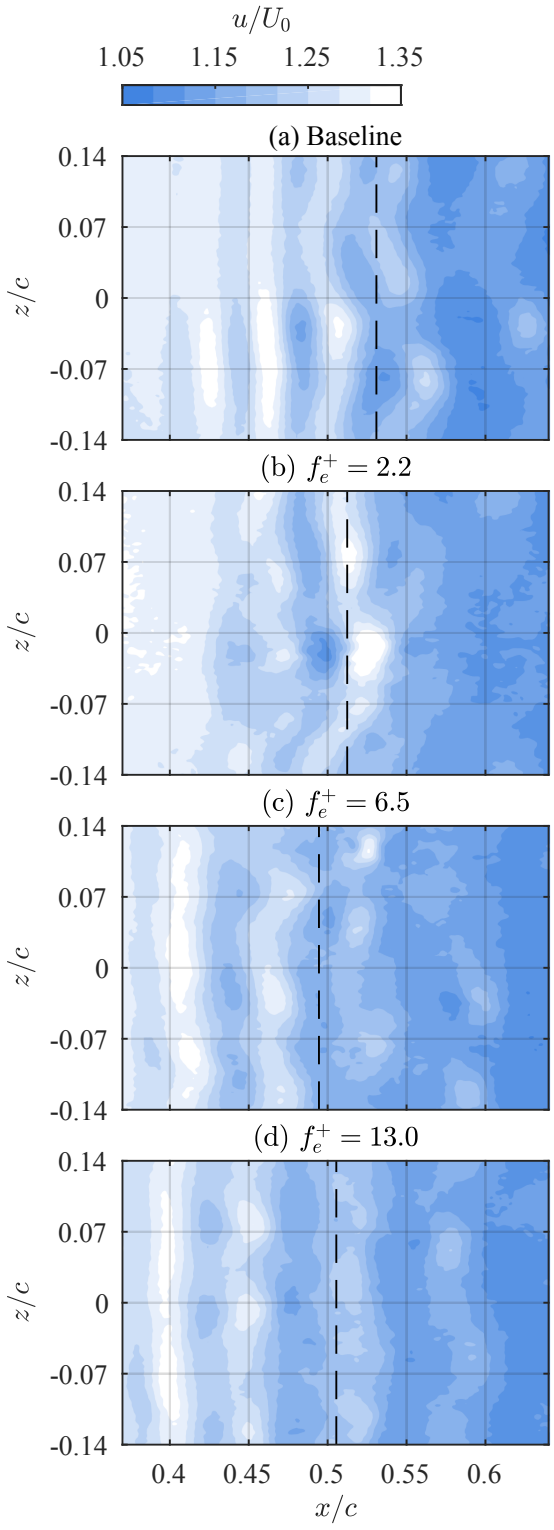

Figure 9: Instantaneous fields of streamwise velocity component on the $x-z$ plane at selected excitation frequencies. The dashed lines indicate the location of mean reattachment.

(figure 8). The spatial modes also indicate lengthening of the characteristic streamwise wavelength of the structures along the streamwise direction.

For excitation at $f_e^+ = 6.5$, the spectra of the temporal coefficient of the first two mode pairs (figure 11d) feature one broad peak centred at a distinct frequency for each mode pair. The dominant amplitude fluctuations of the first two modes are associated with the first harmonic of the excitation frequency, which is close to the most unstable frequency. In conjunction with the corresponding spatial mode, it can be deduced that the first two mode pairs capture the shedding of the dominant spanwise rollers. In contrast to the trend seen for the lower excitation frequencies, the relative energy content of the dominant mode pair increases compared to that for the baseline case (figure 10), suggesting an increased coherence of the shear layer shedding, with the mean shedding frequency matching the first harmonic of the excitation frequency in this case. The amplitude fluctuations of the second mode pair are related to the forcing frequency, which corresponds to approximately half of the most unstable frequency in this case. Strong beating frequencies are also detected in the spectra for both mode pairs, indicative of substantial harmonic interactions [42]. This is reflected in the spatial mode structure pertinent to the second mode pair.

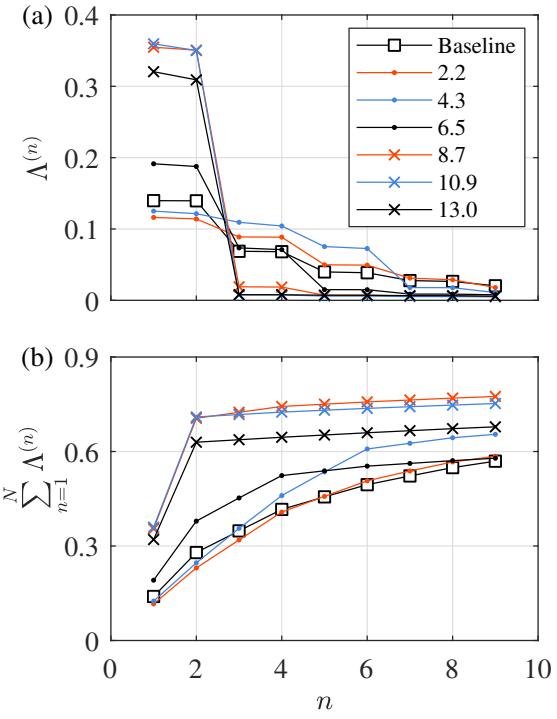

Figure 10: (a) First nine normalised POD eigenvalues, $\Lambda^{(n)} = \lambda^{(n)} / \sum \lambda^{(n)}$ and (b) their cumulative summation.

The shedding process begins to lock onto the excitation frequency when $f_e^+ = 8.7$ (figure 12a). This can be seen from both the topology of spatial mode $\Phi^{(1)}$ and the spectrum of the corresponding temporal coefficient. The second mode pair corresponds to the first harmonic of the excitation frequency, which is within the unstable frequency band predicted by linear stability theory (figure 8a). The locking of the shedding frequency to the excitation frequency is reflected in the significant increase in the relevant energy content of the first two modes, which increases to about 70%, compared to 30% for the baseline case (figure 10). The optimal locking of the shear layer shedding frequency

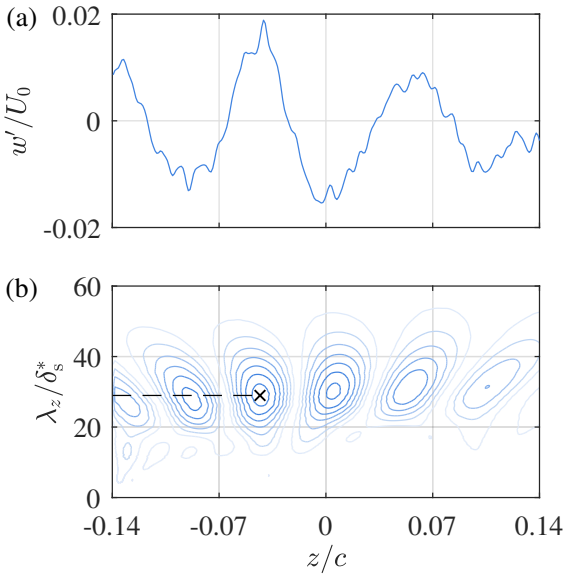

Figure 13: (a) Spanwise distribution of the spanwise velocity fluctuation ($w' = w - \bar{w}$). (b) Wavelet coefficients estimated from the wavelet analysis of the signal in (a). The dashed line demonstrates the spanwise wavelength selection based on the highest value of the wavelet coefficients ($\times$).

is achieved at $f_e^+ = 10.9$ (figure 12b), where both most energetic mode pairs lock onto the excitation frequency. Hereby, the first mode pair reflects the shear layer shedding, capturing over 70% of the fluctuating energy content (figure 10a). Further increase of the excitation frequency to $f_e^+ = 13.0$, shifts the excitation frequency away from the most unstable frequency of the bubble (figure 10a). As a result, while shear layer frequency locking is still achieved (figure 12c), the combined relative energy content of the first two modes decreases compared to that for $f_e^+ = 8.7$ and 10.9 cases. The structure of the second mode pair here relates to subharmonic forcing, and the topology of the corresponding spatial modes (e.g. $\Phi^{(3)}$) is similar to that for $f_e^+ = 6.5$.

3.6. Streamwise and spanwise wavelengths

In order to further gauge the changes imparted on the topological features of vortex shedding by the forcing, the characteristic streamwise wavelength of the main rollers (λ_x) as well as the characteristic wavelength of spanwise deformations (λ_z) of the vortices in the aft portion of the bubble are determined for each forcing case. This is achieved through one-dimensional spatial wavelet analysis [43], performed on top-view velocity measurements. More specifically, the fluctuating components u' and w' are considered for estimating λ_x and λ_z, respectively. The spatial distribution of each aforementioned component is first extracted along the respective dimension (e.g. figure 13a). The highest wavelet coefficient resulting from the convolution of each distribution with the Morlet baseline wavelet function [43] is subsequently used to establish the characteristic wavelength at each time instant (e.g. figure 13b). For improving statistics, this process is repeated across 21 distributed spanwise and streamwise locations for λ_x and λ_z, respectively. Note that the obtained

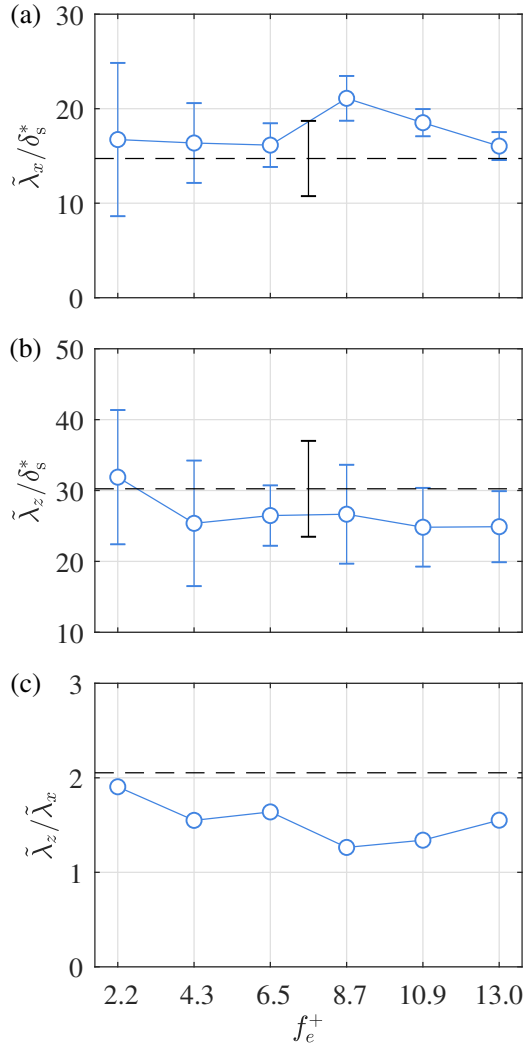

Figure 15: Median streamwise and spanwise characteristic wavelengths for each excitation frequency. The dashed line corresponds to the baseline case while the errorbars are based on $\pm$ one standard deviation.

estimates are based on all measurement realisations, spanning at least 650 shedding cycles.

Figure 14 presents histograms of the estimated characteristic wavelengths for selected forcing frequencies, normalised with the displacement thickness at separation of the unforced bubble, $\delta_s^* = 0.63$mm. In addition, the changes in the median values with excitation frequency are shown in figures 15a and 15b for the streamwise and spanwise wavelength, respectively. The results for the baseline case show that the streamwise wavelength varies by $2\sigma_{\lambda_x/\delta_s^*} = 7.97$, with a median of $\tilde{\lambda}_x/\delta_s^* = 14.73$, closely corresponding with the streamwise period in the first POD mode pair (figure 11a). For a constant convective speed, the range of these values agrees well with a range of frequencies and wavenumbers associated with substantial velocity fluctuations in the separated shear layers identified earlier via spectral analysis (figures 5 and 6). In comparison, a significantly wider variation is seen in the spanwise wavelength of vortex deformations, for which $\tilde{\lambda}_z/\delta_s^* = 30.24$ and $2\sigma_{\lambda_z/\delta_s^*} = 13.53$. Thus, on the average, the ratio of the wavelength median values is

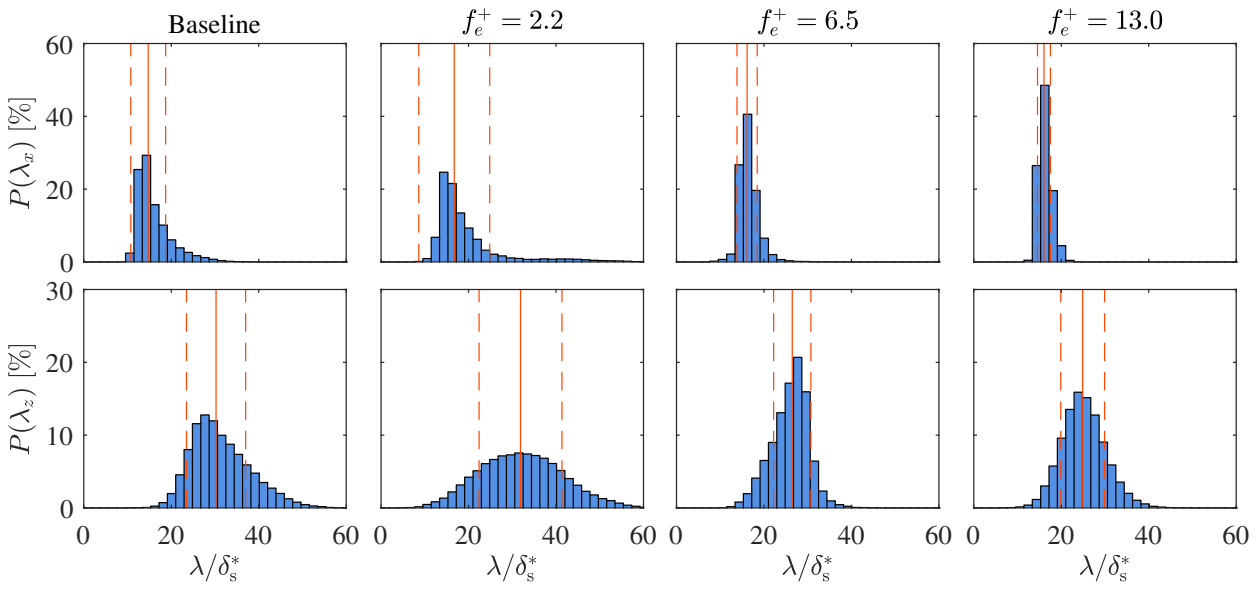

Figure 14: Percentile probability distribution of the estimated streamwise and spanwise wavelengths. Solid and dashed vertical lines correspond to the median and standard deviation limits, respectively.

$\tilde{\lambda}_z/\tilde{\lambda}_x \approx 2.1$, with a similar range of wavelengths ratios reported in previous studies, e.g. 2.4 [8], 2.5 [13] and 2 [19].

When excitation is applied at relatively low frequencies ($f_e^+ = 2.2$ and 4.3), the histogram for λ_x broadens, particularly for the case of $f_e^+ = 2.2$, for which $2\sigma_{\lambda_x/\delta_s^*} = 16.22$ (figure 15). At the same time, the median increases to $\tilde{\lambda}_x/\delta_s^* = 16.74$. The broadening of the histograms agrees with the decrease in the energy content of the first two POD modes for these cases relative to the baseline (figure 10), which is attributed to the modulation of the shedding process by the excitation. The increase in the mean streamwise wavelength is due to the changes in the stability characteristics of the separated shear layer (i.e. growth rate and unstable frequency), a direct consequence of mean flow deformations caused by forcing (figure 8). At these forcing frequencies, the larger cycle-to-cycle variations in the shear layer shedding characteristics lead to larger variability in the wavelength of spanwise deformations, reflected in the broadening of the corresponding histograms in figure 14.

For the particular case of $f_e^+ = 6.5$, the weak lock of shedding to the first harmonic of the excitation frequency evident in figure 11d, leads to an increase in coherence of the shed structures. This is also reflected in the increase of the relative energy content of the most energetic POD mode pair (figure 10). Consequently, the variability in both streamwise and spanwise wavelength of the rollers decreases relative to the baseline case by approximately 70% and 55%, respectively (figure 15). The median streamwise and spanwise wavelengths are $\tilde{\lambda}_x/\delta_s^* = 16.15$ and $\tilde{\lambda}_z/\delta_s^* = 26.47$ ($\tilde{\lambda}_z/\tilde{\lambda}_x = 1.6$), closely corresponding to the observations for the harmonic forcing at $f_e^+ = 13.0$.

By increasing the excitation frequency towards the unstable band, shedding locks to the excitation frequency for $f_e^+ = 8.7$, 10.9, and 13.0. As a result, the variability in the streamwise wavelength, once again, decreases compared to the baseline case (figure 15), correlating with the relative increase in the combined energy content of the first two POD modes (figure 10). The mean wavelength decreases from $\tilde{\lambda}_x/\delta_s^* = 21.10$ for $f_e^+ = 8.7$ to $\tilde{\lambda}_x/\delta_s^* = 16.04$ for $f_e^+ = 13.0$ (figure 15), pertinent to the increasing shedding frequency. The observed increase in the organisation of the shear layer shedding is also accompanied by a proportional decrease in the variability of the characteristic wavelength of spanwise roller deformation. This wavelength falls within $24.89 < \tilde{\lambda}_z/\delta_s^* < 26.66$ for these cases ($f_e^+ = 8.7$, 10.9, 13.0), while the ratio $1.26 < \tilde{\lambda}_z/\tilde{\lambda}_x < 1.55$ varies, following the changes in the mean streamwise wavelength.

Previous investigations have put forth a few hypotheses for the origin of spanwise deformations of the shedding vortex filaments, including possible interaction between the main rollers and weaker streamwise oriented structures originating from the boundary layer upstream of separation [18] and interaction of normal and oblique modes of boundary layer instabilities [19]. The current results provide an experimental quantification of such deformations and explore a possible relation between their characteristic wavelengths and salient features of vortex shedding. To this effect, the data in figures 14 and 15 provide insight into the following aspects of this phenomenon. While the similarity in the median wavelength of spanwise deformations may be linked to preferential growth of perturbations prompted by, for example, microscopic surface imperfections of the model, the results clearly indicate that spanwise deformations occur over a considerable range of wavelengths. Moreover, higher cycle-to-cycle variations in the characteristics of the main vortices, such as for the case of natural transition, lead to a wider spectrum of spanwise wavenumbers. This fact, along with the similarity between the ratio of the streamwise to spanwise wavelengths with approximate estimates from previous studies, suggests a fundamental link between spanwise vortex deformations in laminar separation bubbles and flow stability characteristics governing the development and interaction of perturbations in the boundary

layer and the separated shear layer.

4. Conclusions

This study focuses on the variation in streamwise and spanwise wavelengths pertinent to a laminar separation bubble under natural and periodic excitation conditions. The bubble develops on a NACA0018 airfoil at an angle of attack of 4° and Reynolds number based on chord length of $Re_c = 126,000$. Periodic forcing is achieved by means of an AC-DBD plasma actuator located at 30% of the chord length, upstream of the separation location. Time-resolved particle image velocimetry is employed to independently obtain velocity fields along the streamwise and spanwise planes.

When the bubble is periodically excited, its overall dimensions in the time-averaged sense are reduced. The bubble size variation with excitation frequency closely follows previously reported results [23]. The smallest size is achieved when the forcing frequency is the closest to the most unstable frequency ($f_e^+ \approx 10.9$). The bubble size is directly affecting the stability characteristics determined through linear stability analysis. The latter demonstrate a reduction in the growth rate as the bubble diminishes, in line with the mean flow deformation effects discussed by [3].

When forcing is applied at significantly lower frequencies compared to the most unstable frequency in the separated shear layer, the shear layer shedding is not locked to the excitation frequency but, instead, is modulated. For these frequencies ($2.2 \leq f_e^+ \leq 6.5$) strong amplification of harmonics is evident up to the harmonic nearest to the unexcited bubble fluctuations. By increasing the excitation frequency to values within the unstable frequency band ($f_e^+ \geq 8.7$), vortex shedding locks to the excitation frequency. At the same time, the cycle-to-cycle variations in shedding parameters are significantly reduced while the relative modal energy content of the associated velocity fluctuations increases.

The velocity vector fields of the unexcited bubble along the spanwise plane reveal the formation of uniform spanwise rollers that deform significantly and break down as they convect downstream. Periodic excitation results in earlier shear layer roll-up, leading to the aforementioned reduction in the mean bubble size. For the case of low excitation frequencies, spanwise deformations become more significant. At these frequencies, modulation is reflected in the redistribution of POD modal energy to multiple harmonic modes as compared to the baseline case, with multiple harmonics detected in the frequency spectrum of the corresponding temporal coefficients. On the other hand, when shedding is locked to the excitation frequency, spanwise deformations diminish and the structures break up further downstream. In this case, shedding is captured by the first most energetic POD mode pair and becomes more prevalent in the overall energy content

The characteristic streamwise and spanwise wavelengths are quantified by means of spatial wavelet analysis. Similar to approximate estimates reported in several previous studies [8, 13, 19], the streamwise to spanwise wavelength ratio is 2.1 for the unexcited case. The modulation observed at low excitation frequencies ($f_e^+ = 2.2$ and 4.3) results in increased variation of streamwise wavelengths and a simultaneous increase of the median value with respect to the unexcited case. At the same time, when forcing at the first subharmonic frequency ($f_e^+ = 6.5$) as well as for the cases when locking is achieved ($f_e^+ \geq 8.7$), the shed structures attain increased spanwise coherence. This indicates that spanwise deformations are associated with the prevalent stability characteristics of both the incoming boundary layer as well as of the separated shear layer.

References

[1] M. Gaster, I. Grant, An experimental investigation of the formation and development of a wave packet in a laminar boundary layer, in: Proceedings of the Royal Society of London A: Mathematical, Physical and Engineering Sciences, volume 347, 1975, pp. 253–269.

[2] J. H. Watmuff, Evolution of a wave packet into vortex loops in a laminar separation bubble, Journal of Fluid Mechanics 397 (1999) 119–169.

[3] O. Marxen, U. Rist, Mean flow deformation in a laminar separation bubble: Separation and stability characteristics, Journal of Fluid Mechanics 660 (2010) 37–54.

[4] T. Michelis, M. Kotsonis, S. Yarusevych, Response of a laminar separation bubble to impulsive forcing, Journal of Fluid Mechanics 820 (2017) 633–666.

[5] U. Rist, U. Maucher, Investigations of time-growing instabilities in laminar separation bubbles, European Journal of Mechanics, B/Fluids 21 (2002) 495–509.

[6] S. Yarusevych, P. Sullivan, J. Kawall, Effect of acoustic excitation amplitude on airfoil boundary layer and wake development, AIAA Journal 45 (2007) 760–771.

[7] S. Diwan, O. Ramesh, On the origin of the inflectional instability of a laminar separation bubble, Journal of Fluid Mechanics 629 (2009) 263–298.

[8] O. Marxen, D. S. Henningson, The effect of small-amplitude convective disturbances on the size and bursting of a laminar separation bubble, Journal of Fluid Mechanics 671 (2011) 1–33.

[9] M. Embacher, H. F. Fasel, Direct numerical simulations of laminar separation bubbles: investigation of absolute instability and active flow control of transition to turbulence, Journal of Fluid Mechanics 747 (2014) 141–185.

[10] M. S. H. Boutilier, S. Yarusevych, Separated shear layer transition over an airfoil at a low Reynolds number, Physics of Fluids 24 (2012) 084105.

[11] O. Marxen, M. Lang, U. Rist, Vortex formation and vortex breakup in a laminar separation bubble, Journal of Fluid Mechanics 728 (2013) 58–90.

[12] T. M. Kirk, S. Yarusevych, Vortex shedding within laminar separation bubbles forming over an airfoil, Experiments in Fluids 58 (2017) 43.

[13] J. Kurelek, A. Lambert, S. Yarusevych, Coherent Structures in the Transition Process of a Laminar Separation Bubble, AIAA Journal 54 (2016) 2295–2309.

[14] J. R. Brinkerhoff, M. I. Yaras, Interaction of viscous and inviscid instability modes in separation-bubble transition, Physics of Fluids 23 (2011) 124102.

[15] D. Simoni, M. Ubaldi, P. Zunino, F. Bertini, Transition mechanisms in laminar separation bubbles with and without incoming wakes and synthetic jets, Experiments in Fluids 53 (2012) 173–186.

[16] D. Simoni, D. Lengani, M. Ubaldi, P. Zunino, M. Dellacasagrande, Inspection of the dynamic properties of laminar separation bubbles: free-stream turbulence intensity effects for different Reynolds numbers, Experiments in Fluids 58 (2017) 66.

[17] B. McAuliffe, M. I. Yaras, Transition mechanisms in separation bubbles under lowand elevated-freestream turbulence, Journal of Turbomachinery 132 (2010) 011004.

[18] V. N. Rao, R. Jefferson-Loveday, P. G. Tucker, S. Lardeau, Large Eddy Simulations in Turbines: Influence of Roughness and Free-Stream Turbulence, Flow Turbulence and Combustion 92 (2014) 543–561.

[19] T. Michelis, S. Yarusevych, M. Kotsonis, On the origin of spanwise vortex deformations in laminar separation bubbles, Journal of Fluid Mechanics [Under review] (2018).

[20] E. DeMauro, H. Dell'Orso, S. Zaremski, C. Leong, M. Amitay, Control of Laminar Separation Bubble on NACA 0009 Airfoil Using Electroactive Polymers, AIAA Journal 53 (2015) 2270–2279.

[21] S. Yarusevych, M. Kotsonis, Effect of Local DBD Plasma Actuation on Transition in a Laminar Separation Bubble, Flow, Turbulence and Combustion (2017) 1–22.
[22] L. E. Jones, R. D. Sandberg, N. D. Sandham, Stability and receptivity characteristics of a laminar separation bubble on an aerofoil, Journal of Fluid Mechanics 648 (2010) 257–296.
[23] S. Yarusevych, M. Kotsonis, Steady and transient response of a laminar separation bubble to controlled disturbances, Journal of Fluid Mechanics 813 (2017) 955–990.
[24] S. Burgmann, C. Brücker, A. Schröder, Scanning PIV measurements of a laminar separation bubble, Experiments in Fluids 41 (2006) 319–326.
[25] A. Nati, R. de Kat, F. Scarano, B. W. van Oudheusden, Dynamic pitching effect on a laminar separation bubble, Experiments in Fluids 56 (2015) 172.
[26] S. Pröbsting, S. Yarusevych, Laminar separation bubble development on an airfoil emitting tonal noise, Journal of Fluid Mechanics 780 (2015) 167–191.
[27] T. C. Corke, C. L. Enloe, S. P. Wilkinson, Dielectric barrier discharge plasma actuators for flow control, Annual Review of Fluid Mechanics 42 (2010) 505–529.
[28] T. Michelis, M. Kotsonis, Flow control on a transport truck side mirror using plasma actuators, Journal of Fluids Engineering 137 (2015).
[29] M. Kotsonis, Diagnostics for characterisation of plasma actuators, Measurement Science and Technology 26 (2015).
[30] F. Scarano, M. Riethmuller, Advances in iterative multigrid PIV image processing, Experiments in Fluids 29 (2000) S51–S60.
[31] M. Alam, N. D. Sandham, Direct numerical simulation of "short" laminar separation bubble with turbulent reattachment, Journal of Fluid Mechanics 410 (2000) 1–28.
[32] P. Welch, The use of fast Fourier transform for the estimation of power spectra: A method based on time averaging over short, modified periodograms, IEEE Transactions on Audio and Electroacoustics 15 (1967) 70–73.
[33] U. Rist, K. Augustin, Control of laminar separation bubbles using instability waves, AIAA Journal 44 (2006) 2217–2223.
[34] L. M. Mack, Boundary-layer linear stability theory, Technical Report 709, AGARD, 1984.
[35] J. van Ingen, M. Kotsonis, A two-parameter method for e^N transition prediction, in: 6th AIAA Theoretical Fluid Mechanics Conference, Honolulu, HI, 2011.
[36] D. Simoni, M. Ubaldi, P. Zunino, A simplified model predicting the Kelvin-Helmholtz instability frequency for laminar separated flows, Journal of Turbomachinery 138 (2016).
[37] O. Marxen, R. Kotapati, R. Mital, T. Zaki, Stability analysis of separated flows subject to control by zero-net-mass-flux jet, Physics of Fluids 27 (2015) 024107.
[38] L. Sirovich, Turbulence and the dynamics of coherent structures. I - Coherent structures. II - Symmetries and transformations. III - Dynamics and scaling, Quarterly of Applied Mathematics 45 (1987) 561–571, 573–590.
[39] B. van Oudheusden, F. Scarano, N. Van Hinsberg, D. Watt, Phase-resolved characterization of vortex shedding in the near wake of a square-section cylinder at incidence, Experiments in Fluids 39 (2005) 86–98.
[40] S. Burgmann, A. Schröder, Investigation of the vortex induced unsteadiness of a separation bubble via time-resolved and scanning PIV measurements, Experiments in Fluids 45 (2008) 675–691.
[41] M. Kotsonis, L. Veldhuis, Experimental study on dielectric barrier discharge actuators operating in pulse mode, Journal of Applied Physics 108 (2010) 113304.
[42] R. W. Miksad, Experiments on the nonlinear stages of free-shear-layer transition, Journal of Fluid Mechanics 56 (1972) 695–719.
[43] I. Daubechies, Ten Lectures on Wavelets, volume 61 of *CBMS-NSF Regional Conference Series in Applied Mathematics*, SIAM, 1992.

*Highlights

1. At excitation frequencies below the unstable frequency band, the shear layer does not lock to the excitation but is, instead, modulated.

2. Excitation within the unstable frequency band locks the shear layer shedding.

3. For modulated shedding, spanwise deformations become more significant than in the natural case.

4. For locked shedding, coherence of the rollers along the span increases.